Article

Enhanced Activation of Peroxymonosulfate via Sulfate Radicals and Singlet Oxygen by $SrCo_xMn_{1-x}O_3$ Perovskites for the Degradation of Rhodamine B

Penghui Shao [1,2], Xiping Yin [2], Chenyu Yu [2], Shuai Han [2,*], Baohuai Zhao [2], Kezhi Li [2], Xiang Li [1,*],
Zhenyu Yang [2], Zhiwei Yuan [2], Qinzhi Shi [2], Jing Ren [2], Haiqiang Hu [2], Kai Cui [2], Tengfei Li [2] and Jun Jiang [2]

[1] College of Chemical Engineering and Materials Science, Tianjin University of Science and Technology, Tianjin 300457, China
[2] Institute of Engineering Technology, Sinopec Catalyst Co., Ltd., Beijing 100029, China
* Correspondence: hansjz.chji@sinopec.com (S.H.); lixiang@tust.edu.cn (X.L.)

Abstract: Perovskite is of burgeoning interest in catalysis, principally due to such material having high thermal stability, modifiable variability, ferromagnetism, and excellent catalytic performance in peroxomonosulfate (PMS) activation. In this study, the $SrCo_xMn_{1-x}O_3$ perovskites with different Mn doping were synthesized by a facile sol-gel method for peroxymonosulfate (PMS) activation to degrade Rhodamine B. The obtained $SrCo_{0.5}Mn_{0.5}O_3$ perovskite exhibited the best catalytic efficiency, as Rhodamine B (40 mg/L) was removed completely within 30 min. In the system of $SrCo_{0.5}Mn_{0.5}O_3$–PMS, several reactive species were produced, among which sulfate radicals and the singlet oxygen mainly contributed to Rhodamine B degradation. The relatively high catalytic performance could be attributed to the coupled redox cycle between Mn and Co, and the abundant oxygen vacancies. Moreover, the $SrCo_{0.5}Mn_{0.5}O_3$ catalyst showed excellent stability and reusability, maintaining a high catalytic activity after several cycling tests. This study demonstrated that the Mn doping of $SrCoO_3$ could not only enhance the B-site activation in $SrCo_{0.5}Mn_{0.5}O_3$ but also enrich the oxygen vacancies, thus improving the efficiency of PMS activation.

Keywords: PMS; perovskite; degradation of RhB; oxygen vacancy; wastewater treatment

1. Introduction

Organically synthetic dyes have been used widely in people's daily lives with the increase of industrialization, along with the increased demand for products related to fiber-material products, printing, papermaking, medicine, and information materials industries. Dyes are also used to make dye-sensitized solar cells with potentially high photoelectric conversion efficiency to promote a greener energy transition [1,2]. It is noted that these highly stable industries are, by nature, usually toxic and carcinogenic, which poses a great threat to the environment and human health [3–5]. As a representative contaminant, Rhodamine B (RhB) ($C_{28}H_{31}ClN_2O_3$) has a high water solubility and carcinogenicity hazard [6]. To treat such contaminants, advanced oxidation processes (AOPs) have been investigated widely as an effective approach due to their excellent oxidation performance [7–9].

Compared with the traditional AOPs, sulfate radical-based AOPs (SR-AOPs) have gradually become promising technologies in water treatment due to their strong oxidation ability in a wide pH range [10–13]. Typically speaking, sulfate radicals ($SO_4^{-\cdot}$) generated in the activation of PMS have a higher standard reduction potential (E_0 = 2.5–3.1 V) [14,15] and better selectivity for most refractory organic pollutants [16,17]. Though homogeneous catalysts performed excellent PMS activation, the transition metal ions are a serious threat to the ecosystem and a risk of secondary pollution [18]. Hence, the activation of PMS by catalysts was considered a feasible method for the degradation of contaminants due to its economical, reusability, and operational simplicity [19,20]. In addition, it avoided

the secondary pollution caused by toxic metal ions to a certain extent. Among these, the perovskite catalysts/PMS system has drawn great attention due to its feasibility to be separated from the water originating from its ferromagnetism, and modifiable variability by its abundant structure modification possibility [21–23].

Perovskite has a typical structure of ABO_3, and various elements with potent redox properties could be chosen to reside in A or B sites [24], thus providing the feasibility to modify its catalytic property [25]. For simple ABO_3 perovskite, it was reported that $SrCoO_3$ and $LaCoO_3$ perovskite exhibited a higher activity under the PMS activation for phenol degradation [26]. Meanwhile, common transition elements such as Co, Mn, and Fe constructed as a B site show high efficiencies towards SR-AOPs [27–29]. Co-based perovskites are investigated as a PMS activator with widespread attribution of the redox compatibility and impressive PMS activation by Co species [23,30]. Mn-based perovskites usually show unique performance on PMS activation due to the high surface area, the multivalence nature of Mn ions, and the oxygen defects [31,32].

To further improve the perovskite performance, a third metal cation can be doped in the B site to control the oxidation states of the original element and obtain more oxygen vacancies [33–35]. For example, the bimetallic synergistic doping of Co and Fe in $LaCo_{0.5}Fe_{0.5}O_3$ exhibited an impressive removal efficiency of bisphenol A(BPA) [29]. The Cu-substituted $LaFeO_3$ perovskite not only created a metal redox cycle between Fe^{3+} and Cu^+ but also increased the amount of the surface hydroxyl groups [36]. The reactive oxygen species in layered perovskite $LaSrCo_{0.8}Fe_{0.8}O_4$ facilitates the formation of nonfree radical singlet oxygen, which shows exceptionally efficient PMS activation [37]. Therefore, to enhance the PMS activation, based on achieving more oxygen vacancies and accelerating the redox cycling of the transition metals, we tried to synthesize the $SrCo_xMn_{1-x}O_3$ perovskites and explore the effect of Mn on the B site.

In this paper, $SrCo_xMn_{1-x}O_3$ perovskite was synthesized by the facile sol-gel method. RhB was selected as the target pollutant to examine the activation of PMS under the affection of the catalyst. The reaction conditions such as PMS concentration, catalyst dosage, pH, reusability, and stability were also explored. Furthermore, the mechanism of the interaction between the singlet oxygen and the persulfate radical was confirmed in $SrCo_{0.5}Mn_{0.5}O_3$–PMS system by EPR and quenching experiments. The $SrCo_{0.5}Mn_{0.5}O_3$ perovskite was found to have more oxygen vacancies and show superior catalyst activation and stability with the doping of Mn in this study. The $SrCo_{0.5}Mn_{0.5}O_3$–PMS system would be a promising candidate to degrade RhB in wastewater treatment.

2. Experiment

2.1. Materials

All reagents in the experiment were of analytical grade. Strontium nitrate, tert-butanol, and citric acid monohydrate were from Xi Long Scientific(Beijing, China). Cobalt nitrate hexahydrate ($Co(NO_3)_2·6H_2O$), and 50% manganese nitrate solution ($Mn(NO_3)_2·50$ wt%) were from Tianjin Da Mao Chemical Reagent Factory(Tianjin, China). PMS ($2KHSO_5·KHSO_4·K_2SO_4$), p-benzoquinone, L-histidine, and sodium thiosulfate were from Macklin(Shanghai, China). The Rhodamine B was from Tianjin Fuchen Chemical Reagent Factory(Tianjin, China). The solution pH was adjusted by a 0.1 M H_2SO_4 or NaOH solution. Deionized water was used throughout the work.

2.2. Preparation of Catalysts

$SrCo_xMn_{1-x}O_3$ perovskites were synthesized via the sol-gel method using citric acid as an organic complexing agent. For a typical synthesis of $SrCoO_3$, citric acid, strontium nitrate, and cobalt nitrate hexahydrate were poured into the beaker sequentially and stirred vigorously (450 rpm), then continuously heated to 90 °C until the total evaporation of the solvent. The resulting powder was dried at 110 °C overnight and calcined at 900 °C for 5 h with a heating rate of 2 °C min^{-1}. For the $SrCo_xMn_{1-x}O_3$ perovskites, manganese nitrate

as another B-site component was added to the mixed solution as a certain molar ratio ($x = 0$, 0.3, 0.5, 0.6,0.7, 0.8, 0.9, and 1.0, respectively).

2.3. Characterization of Catalysts

X-ray diffraction (XRD) patterns of all perovskite catalysts were characterized by the X-ray diffractometer (Smart Lab, Rigaku, Japan) with Cu Kα line as the source (60 kV, 150 mA) and the scanning range (2θ) was from $10°$ to $90°$. The elemental compositions of the samples were analyzed by X-ray fluorescence spectroscopy (ZSX PrimusIV). Scanning electron microscopy (SEM) was applied to observe the morphology and structure of the perovskites by Gemini SEM 300 (ZEISS, Germany). Energy dispersive spectroscopic (EDS) mapping was also applied to verify the uniformity of the element. To analyze the specific surface areas and the pore-size distributions, nitrogen physisorption was performed on a Micromeritics ASAP 2460 analyzer. The leaching volume of catalysts was determined by ICPE-9820 (Shimadzu, Japan). The concentration of RhB was all obtained by UV-Vis-2600i. The oxygen defect was determined by electron paramagnetic resonance (EPR) at 9.853 GHz by EMXPlus. For O_2-TPD (temperature programmed desorption) (AMI-300IR), the perovskites were treated at 500 °C for 1 h in an oxygen atmosphere. Then, the cooled perovskites purged by argon were heated to 900 °C under a constant argon flow, with a flow rate of 30 mL/min and a heating rate of 10 °C min^{-1}. To confirm the synthesis of the perovskites, the FT-IR was measured by Thermo Fisher Nicolet Is5 in a wave number from 400–2000 cm^{-1}. X-ray photoelectron spectroscopy (XPS, Thermo ESCALAB 250XI) was applied to obtain the chemical valence of fresh and used catalysts. All the binding energies were calibrated with C 1 s peak at 284.8 eV. Radicals in the system were identified by the EPR test (Bruker EMXplus) with the DMPO and TEMP as the spin-trapping agents.

2.4. Catalytic Activity Measurements

In the typical experiment, Rhodamine B (RhB) was selected as a target pollutant to evaluate the catalyst activity. The concentration of RhB was tested by a UV-Vis spectrophotometer based on the Lambert-Beer law. Experiments were carried out in a 300 mL beaker with 250 mL 40 mg/L RhB solution with continuous stirring at 300 rpm in the magnetic stirrer. The specific number of $SrCo_xMn_{1-x}O_3$ catalysts was added into the breaker and stirred for 30 min to reach adsorption equilibrium. When the concentration of RhB reached equilibrium, certain amounts of PMS were added to the solution. The initial pH (3–9) was adjusted by a 0.1 M H_2SO_4 or 0.1 M NaOH solution and the temperature was held at 25 °C. At the specified time point, about 2.5 mL of the reaction solutions were withdrawn through a 0.22 μm membrane filter and quenched immediately with 40 μL 0.1 M $Na_2S_2O_3$ solution. The collected perovskites were analyzed by the UV-VIS-2600i (Shimadzu Japan) to obtain the removal efficiency of the RhB. Different dosages of catalysts and PMS were studied to obtain the optimal reaction conditions. The recycling experiments were also performed to investigate the reusability and stability of the catalyst. The used perovskite catalyst was washed with deionized water and ethanol three times in sequence and dried overnight at 80 °C in the oven. And the leaching of Co and Mn cations was measured by ICP spectrometry. To confirm the dominant reactive radicals in the $SrCo_{0.5}Mn_{0.5}O_3$–PMS system, tert-butanol, p-benzoquinone, methanol, and L-histidine were used as quenching agents for the different active radicals respectively.

3. Results and Discussion

3.1. Characterization of Catalysts

The actual substitution of Mn was analyzed by XRF and listed in Table 1. For the $SrCo_xMn_{1-x}O_3$ perovskites, the actual metal content was consistent with the named content. To analyze the crystal structure of the perovskites, an XRD analysis was conducted, as shown in Figure 1a. According to the X-ray powder diffraction patterns of the $SrCo_xMn_{1-x}O_3$ perovskites, the $SrCoO_3$ perovskite phase (JCPDS number 49-0692) and the $SrMnO_3$ (JCPDS number 24-1213) were observed [38]. From Figure 1b, the shift of diffrac-

tion peaks to a lower angle suggests the dope of Mn inside $SrCoO_x$, which enlarges the unit cell parameters due to its larger ionic radius (Mn^{3+}: 0.66 Å, Co^{3+}: 0.63Å). It indirectly proved that manganese was doped into the perovskite lattice. From Table S1, the lattice parameters decreased with the Mn doping, which may be caused by the formation of anion defects [39]. It is worth highlighting that when the Co:Mn ratio decreased to 3:7, it had an obvious superposition of the diffraction peaks of $SrCoO_3$ and $SrMnO_3$. Meanwhile, the characteristic of $SrMnO_3$ was weaker than $SrCoO_3$, which may be explained by the following two aspects: better affinity for the forming perovskite phase and the Mn phase hinders the decomposition of carbonate [40,41]. These results implied that Mn can be doped into the $SrCoO_3$ perovskite partially and eventually become a mixture with the increase of Mn. Additionally, the detailed $SrCo_xMn_{1-x}O_3$ perovskites were characterized by XRD (Figure S1).

Table 1. The actual composition of $SrCo_xMn_{1-x}O_3$ perovskites.

Perovskites	Metal Content (Atomic)	
	Co	Mn
$SrCo_{0.7}Mn_{0.3}O_3$	0.71	0.29
$SrCo_{0.5}Mn_{0.5}O_3$	0.52	0.48
$SrCo_{0.3}Mn_{0.7}O_3$	0.33	0.67
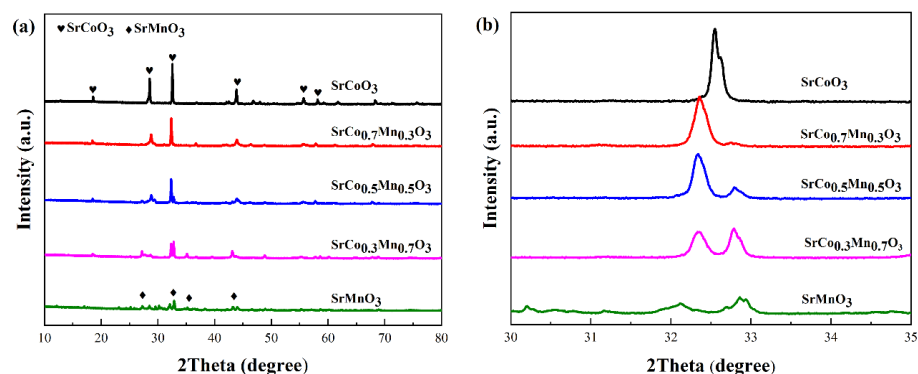
Figure 1. (**a**) XRD patterns of the $SrCo_xMn_{1-x}O_3$ perovskites. (**b**) A comparison with the pattern of the $SrCo_xMn_{1-x}O_3$ perovskites.

As in Table 2, the specific surface area of $SrCoO_3$ was small, which is a typical property for perovskite materials [42,43], which may be attributed to the high synthesis temperature. With the addition of Mn, though the specific surface area of $SrCo_xMn_{1-x}O_3$ increased from 0.63 m^2/g to 4.21 m^2/g, all perovskites demonstrated a small surface area, which presumed the key factors of the difference regarding their catalytic activity was not the surface area. Details of the surface texture of the catalysts are listed in Table S1 and the typical nitrogen adsorption-desorption isotherm is shown in Figure S2, where it can be seen that the $SrCo_xMn_{1-x}O_3$ perovskites did not change much in pore volume and pore size.

Table 2. BET surface area, total pore volume, and average pore diameter of the $SrCo_xMn_{1-x}O_3$ perovskites.

Perovskites	SSR (m^2/g)	Pore Volume (cm^3/g)	Average Pore Size (nm)
$SrCoO_3$	0.63	0.002	12.2
$SrCo_{0.7}Mn_{0.3}O_3$	3.05	0.011	13.9
$SrCo_{0.5}Mn_{0.5}O_3$	3.33	0.009	11.9
$SrCo_{0.3}Mn_{0.7}O_3$	4.21	0.016	17.2
$SrMnO_3$	4.11	0.016	17.2

The particulate morphology of $SrCo_xMn_{1-x}O_3$ was examined by SEM. From Figure 2, it can be found that when compared with the Mn-replaced $SrCo_xMn_{1-x}O_3$ perovskites, the $SrCoO_3$ perovskites have more severe particle aggregation. EDS element mappings clearly showed a uniform distribution of Sr, Mn, Co, and O on the $SrCo_{0.5}Mn_{0.5}O_3$ (Figure 2g). Moreover, the EDS results obtained from a microzone (Figure S3) are consistent with those obtained by XRF to further prove the uniform distribution at a microscale.
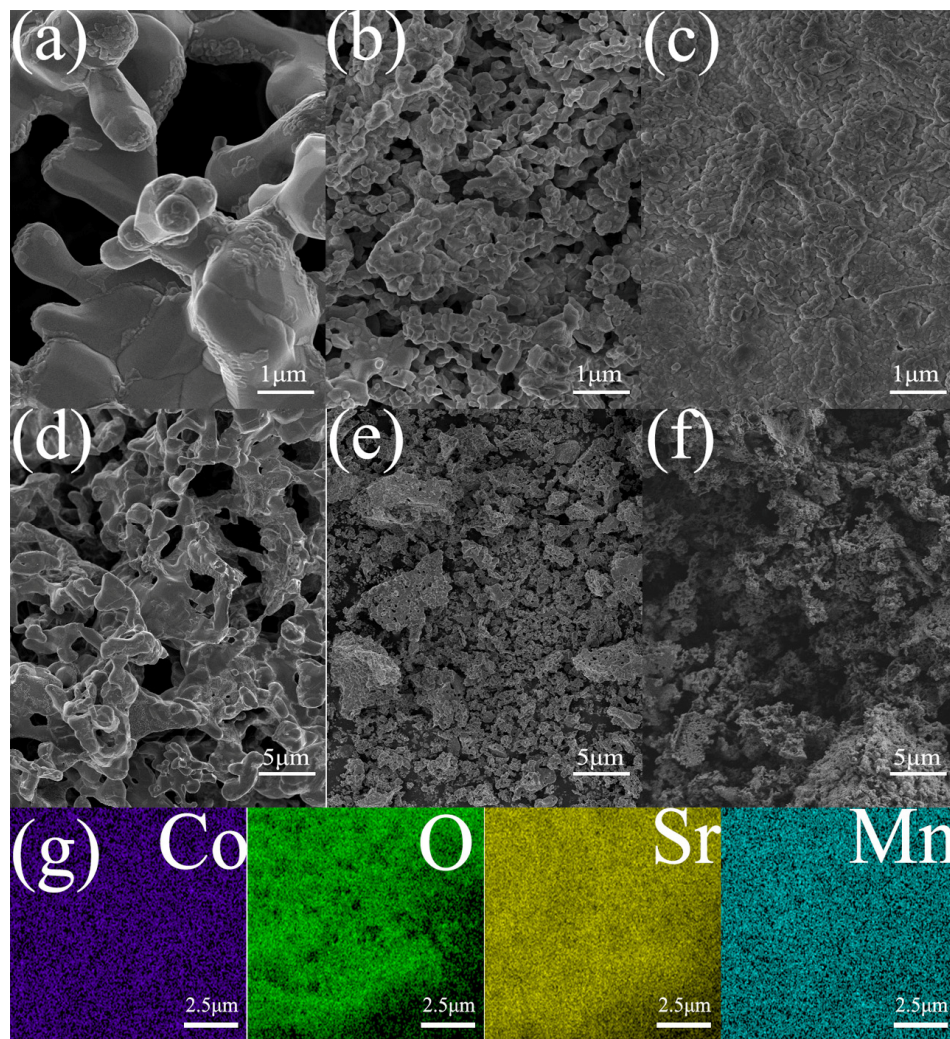

Figure 2. The 1μm and 5μm SEM images of $SrCo_xMn_{1-x}O_3$. (**a**,**d**) $SrCoO_3$, (**b**,**e**) $SrCo_{0.5}Mn_{0.5}O_3$, (**c**,**f**) $SrMnO_3$ perovskites; (**g**) EDS spectra of $SrCo_{0.5}Mn_{0.5}O_3$.

3.2. Active Oxygen Species Analysis

Catalyst-assisted SR-AOPs are related to the activation ability of oxygen-related intermediates in reaction. O_2-TPD experiments were applied to study the oxygen species in different Mn-substituted perovskites. As depicted in Figure 3a, the characteristic peaks of oxygen that evolved from the $SrCo_xMn_{1-x}O_3$ perovskites mainly appeared at high temperatures (>800 °C), which resulted from the lattice oxygen species [44]. There are no obvious signal peaks of surface weakly adsorbed oxygen from 200 to 500 °C, which corresponded to the very-low specific surface area [45,46]. With the increase of Mn-substitution, the amount of oxygen released from the lattice oxygen gradually increased [47]. As a whole, there was no obvious difference in lattice oxygen among the perovskites.
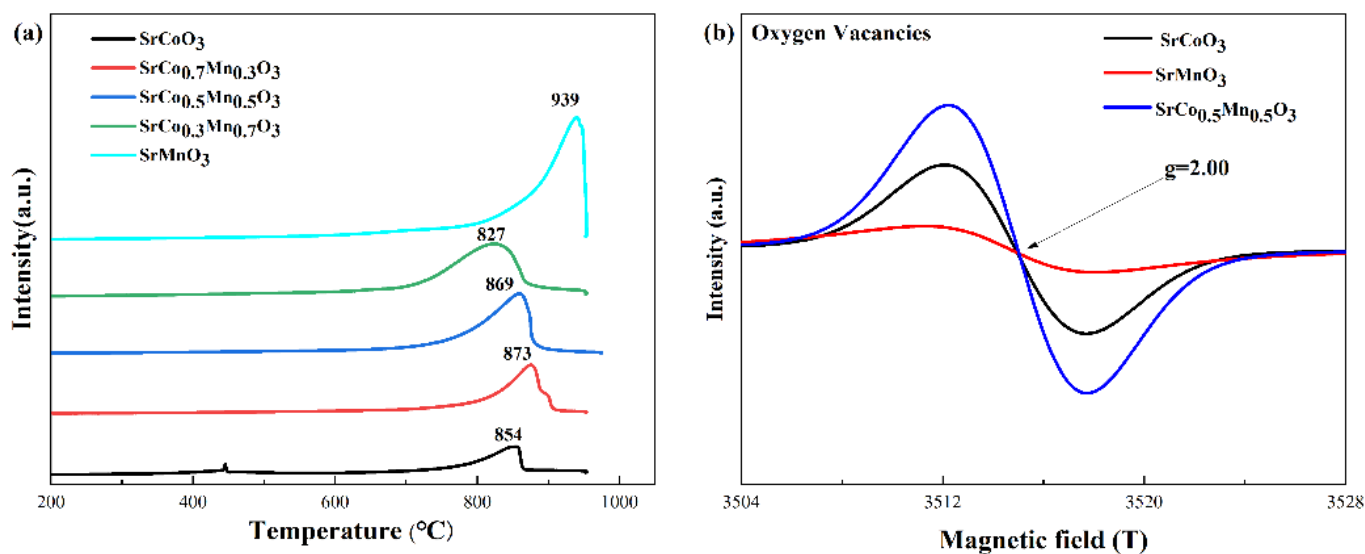
Figure 3. (**a**) O_2-TPD of $SrCo_xMn_{1-x}O_3$ perovskites. (**b**) EPR spectra of $SrCo_xMn_{1-x}O_3$ perovskites.

In addition to the existing oxygen species, metal oxides usually consisted of active oxygen vacancies, which could promote the activation of oxygen-related precursors. Perovskites are typically active in redox reactions partially due to their abundant oxygen vacancies, especially when rationally doped. Oxygen vacancy was characterized by the EPR technique to investigate the variation caused by the dope of Mn. As shown in Figure 3b, the centrally symmetrical signals at the *g* factor of 2.00 were ascribed to the oxygen vacancies. The strongest signal from $SrCo_{0.5}Mn_{0.5}O_3$ perovskite illustrated that the substitution of Mn led to more oxygen vacancies. The result was attributed to the Mn doping leads distortion in the Co-O octahedra and weaker metal-oxygen bonds, which reduced the formation of oxygen vacancies [40]. In comparison, $SrCoO_3$ and $SrMnO_3$ all showed a lesser amount of oxygen vacancies, which proved the promotion effect of oxygen vacancy generation by Mn doping.

3.3. The Catalytic Activity of Catalysts

As a typical dye contaminant in wastewater, RhB was selected to evaluate the catalytic performance of perovskites for the activation of PMS. From Figure S5, sole PMS could oxidize only 10% of RhB, and the absorption capability of $SrCoO_3$ (without PMS) for RhB was limited (only 10%) in 30 min, meaning the sole PMS or perovskite catalyst could only contribute in a limited way to the removal of RhB. When PMS was added simultaneously with $SrCo_xMn_{1-x}O_3$, the concentration of RhB was reduced to close to zero within 25 min (Figure 4a), which showed that all $SrCo_xMn_{1-x}O_3$ perovskites had high efficiency for PMS activation.

The catalytic degradation activity of RhB using different $SrCo_xMn_{1-x}O_3$ (*x* from zero to one) activating PMS is shown in Figure 4a. Compared to the pure perovskites with only Mn or Co cations, it can be seen that the B site doped perovskites showed much higher catalytic performance. From Table 3, the degradation kinetics of RhB in different perovskites/PMS was shown by applying the first-order kinetics, which were as below:
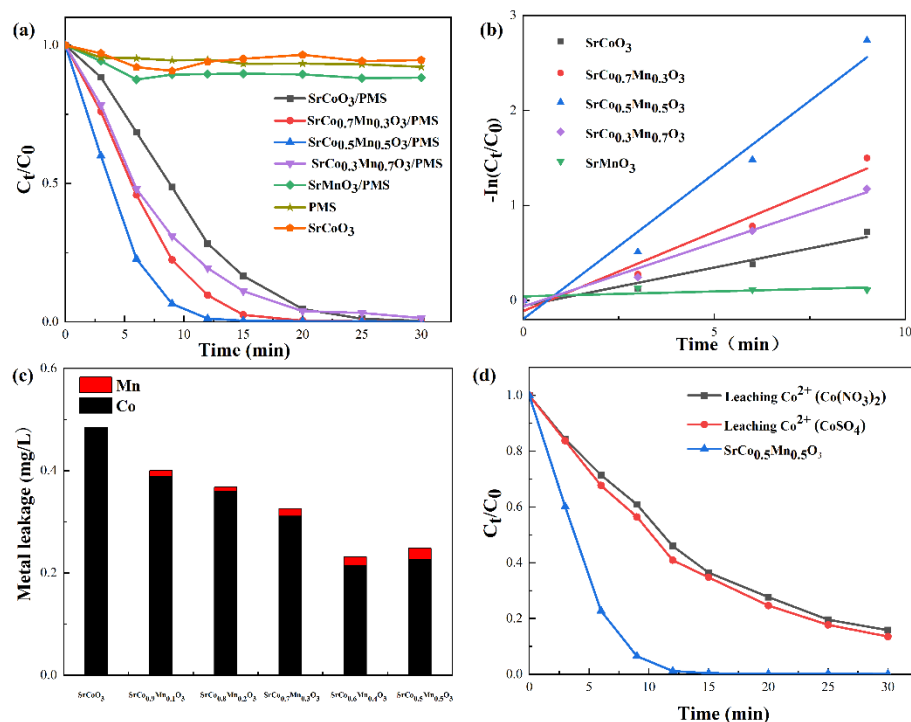
$$-\ln(C_t/C_0) = kt$$

Figure 4. (**a**) Degradation efficiency of RhB in the presence of $SrCo_xMn_{1-x}O_3$ perovskites. Reaction conditions: PMS:0.06mM, catalysts:0.06g L^{-1}, 298 K, pH = 7. (**b**) Degradation efficiency of RhB in the presence of $SrCo_xMn_{1-x}O_3$ perovskites. (**c**) Leaching concentration of Co and Mn of $SrCo_xMn_{1-x}O_3$ perovskites. (**d**) The degradation efficiency of RhB in the Co^{2+}–PMS system.

Table 3. Summary of different catalysts–PMS systems for removing RhB.

Catalysts	Conditions			Degradation	Main Active Species	Ion Leaching/ mg L^{-1}	Ref.
	PMS Conc/mM	RhB Conc/mg L^{-1}	Catalyst Dose/g L^{-1}				
Co-NC-850	0.800	80.00	0.025	20 min 100%	Co	25	[48]
LMO-5bar-600	4.900	20.00	0.200	45 min 100%	Mn	0.200	[49]
$NiCo_2O_4$	0.500	23.95	0.200	20 min 95%	Co Ni	-	[50]
Co/N-NPC$_{0.5/900}$	1.250	9.58	0.005	10 min 100%	Co	0.408	[51]
$ZnCo_2O_4$	0.049	10.00	0.030	30 min 100%	Co	0.220	[52]
Co@DC	0.160	10.00	0.020	5 min 100%	Co	0.840	[53]
Fe/Co-N/P-9	0.650	40.00	0.060	35 min 98.31%	C-π, Co, Fe.	-	[54]
Mn-Fe-CN	0.320	25.00	0.100	12 min 100%	Fe	0.600	[55]
$SrCo_{0.5}Mn_{0.5}O_3$	0.060	40.00	0.060	15 min 100%	Co Mn	0.220	This work

The catalytic-activity kinetic constant of $SrCo_{0.5}Mn_{0.5}O_3$ (k = 0.306 min^{-1}) was the highest among all the catalysts, with an order of magnitude higher than the undoped $SrCoO_3$ (k = 0.081 min^{-1}) perovskites. Meanwhile, it can be observed that the kinetic constant of RhB degradation on $SrCo_{0.5}Mn_{0.5}O_3$ was 3.78 and 30.6 times that of the $SrCoO_3$ and $SrMnO_3$ perovskites. Therefore, the catalytic performance of $SrCo_{0.5}Mn_{0.5}O_3$ should be attributed to the doping effect of Mn, since the $SrMnO_3$ phase had a poor catalytic performance even worse than its counterpart $SrCoO_3$.

Another factor to consider in the actual environment is the stability of the catalyst. The dissolution of the active centers usually leads to the failure of the catalyst in routine running. The leaching experiment was applied to monitor the stability test. As in Figure 4c, Mn is stable for all the catalysts compared with Co, and the leaching of the cobalt cation in $SrCo_{0.5}Mn_{0.5}O_3$–PMS was only 0.22mg/L after the reaction (30 min), which was less than

half of that in the SrCoO$_3$–PMS system (Figure 4c). Therefore, the SrCo$_{0.5}$Mn$_{0.5}$O$_3$ catalyst exhibits good catalytic activity and stability.

To further analyze the possible function of the dissolved Co^{2+}, an exact concentration of Co^{2+} (0.22 mg/L) originated from CoSO$_4$ and Co(NO$_3$)$_2$ was investigated under the same degradation experiment system, without adding any solid catalysts. As shown in Figure 4d, compared to the SrCo$_{0.5}$Mn$_{0.5}$O$_3$–PMS system, the simulated leached Co^{2+} cases show relatively worse reactivity, with only 85% of the RhB removed in 30 min. Taking into account that the actual concentration of Co^{2+} leached was much less than in the simulated cases, it can be indicated that the heterogeneous reaction had a fundamental effect on the system.

To further investigate the stability and reusability of the catalyst, four consecutive degradation experiments were conducted. As displayed in Figure 5, the removal of RhB maintained 94% at 30 min after the 4th cycle, which exhibited good reusability for SrCo$_{0.5}$Mn$_{0.5}$O$_3$ perovskite.

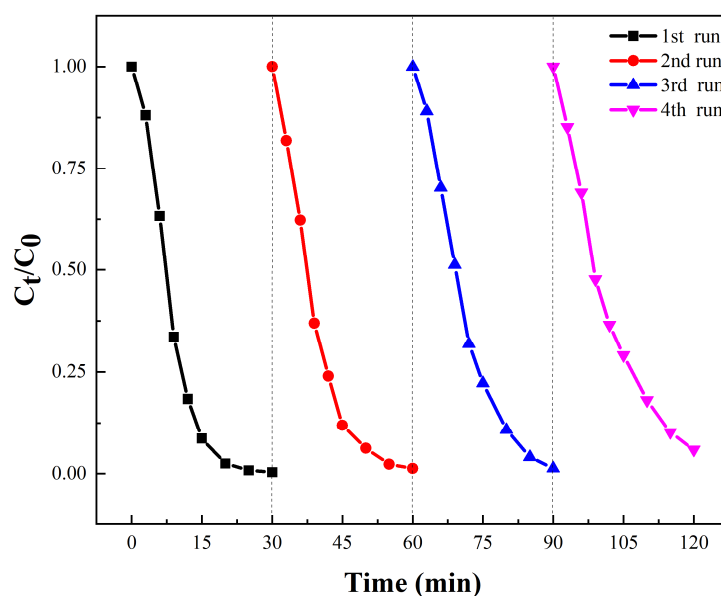**Figure 5.** Reusability of SrCo$_{0.5}$Mn$_{0.5}$O$_3$ for the degradation of RhB. Reaction conditions: [RhB] = 40 mg L^{-1}, [PMS] = 0.06 mM, catalysts = 0.03 g L^{-1}, T = 298 K.

Furthermore, to evaluate the overall performance of SrCo$_{0.5}$Mn$_{0.5}$O$_3$–PMS for removing RhB, a comparison of several typical catalysts for PMS activation was summarized in Table 3. In this work, SrCo$_{0.5}$Mn$_{0.5}$O$_3$ showed a very high activation ability for PMS and catalyst stability.

3.4. Effect of Reaction Parameters on RhB Degradation

The effect of various operation factors in the SrCo$_{0.5}$Mn$_{0.5}$O$_3$–PMS system for the removal of RhB, including PMS concentration, the dosage of SrCo$_{0.5}$Mn$_{0.5}$O$_3$, and pH, were investigated to illustrate the relationship between the operation and degradation efficiencies.

As shown in Figure 6a, when the catalyst concentration was increased from 0.015 g/L to 0.030 g/L, it can be observed that the removal efficiency of RhB was significantly enhanced from 69.8% to 100.0% within 30 min. The phenomenon was likely attributed to more active radicals generated from more SrCo$_{0.5}$Mn$_{0.5}$O$_3$ perovskite. However, when the catalyst concentration was increased from 0.045 g/L and 0.06 g/L, the degradation rates of RhB maintained almost the same, since PMS might exhibit a self-quenching effect caused by excess metal species and radicals.
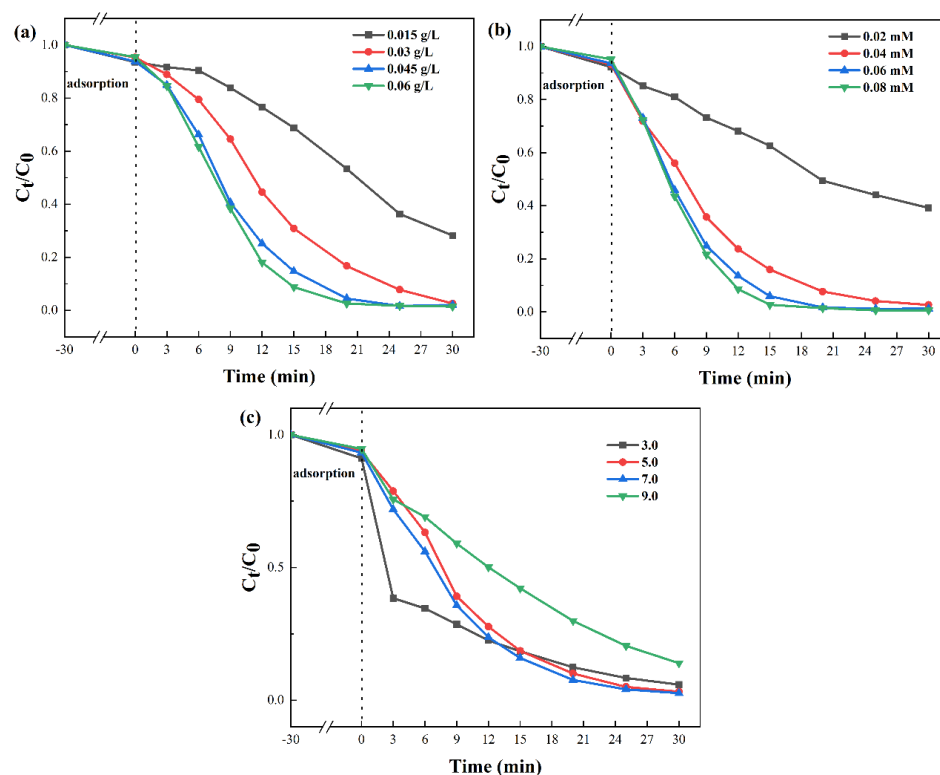
Figure 6. Effects of (**a**) catalyst dosage, (**b**) PMS concentration, and (**c**) pH on RhB degradation in $SrCo_{0.5}Mn_{0.5}O_3-$PMS (PMS: 0.04 mM). Reaction conditions: RhB: 40 mg L^{-1}, PMS: 0.06 mM, $SrCo_{0.5}Mn_{0.5}O_3$: 0.03 g L^{-1}, unless otherwise noted. T: 298.15 K. pH: nature.

The influence of PMS concentration on the degradation efficiency of RhB was further explored. As in Figure 6b, the general trend displayed that the PMS concentration (0.02 mM to 0.04 mM) had a significant enhancement effect on RhB degradation. When the PMS concentration further changed from 0.04 mM to 0.08 mM, the removal efficiency of RhB showed only a slight ascent, from 90% to 100%, within 25 min. It can be ascribed to the self quenching of the generated radicals with PMS [56,57] by Equations (1) and (2).

$$SO_4^{-\cdot} + HSO_5^- \rightarrow HSO_4^- + SO_5^{-\cdot} \tag{1}$$

$$\cdot OH + HSO_5^- \rightarrow SO_5^{-\cdot} + H_2O \tag{2}$$
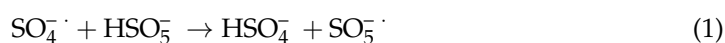
The initial pH has played a vital role in the degradation of RhB by the $SrCo_{0.5}Mn_{0.5}O_3-$PMS system, as shown in Figure 6c. The perovskites maintained a high catalytic performance as the initial pH ranged from three to seven, though the removal efficiency did not perform well at the initial pH of nine (85.6% within 30 min), which may be attributed to the fact that the generation of $SO_4^{-\cdot}$ was inhibited under alkaline conditions. As shown in Figure S6, the pH_{zvc} of $SrCo_{0.5}Mn_{0.5}O_3$ was 7.83. $SrCo_{0.5}Mn_{0.5}O_3$ perovskite is negatively charged when the intimal pH > 7.83 is a hinderance to the activation of PMS due to the repulsive force [58]. A significant drop in the removal efficiency of RhB in the first three minutes (47%) can be observed at an initial pH of three. This observation can be attributed to the fact that the protonated surfaces on the catalytic are easier to adsorb HSO_5^- and generate much more radicals.

3.5. Identification of Mainly Reactive Species in the $SrCo_{0.5}Mn_{0.5}O_3$–PMS System

Overall, the degradation of RhB has two paths: chromophore-structure destruction and deethylation [49]. From the UV-VIS spectra (Figure S7), the characteristic peak did not blue shift or red shift, which showed the cleavage of the whole conjugated chromophore

structure of RhB is easier than the deethylation process. Thus, the radicals mainly contributed to the chromophore-structure destruction.

To identify the main reactive radicals, quenching experiments were conducted in the $SrCo_{0.5}Mn_{0.5}O_3$–PMS system. As is commonly suggested in SR-AOPs, four types of reactive radicals could be generated in the activation of PMS, including peroxy-sulfate, hydroxyl radical ($\cdot OH$), singlet oxygen ($^1O_2$), and superoxide radical($O_2^{-}\cdot$) [14]. As shown in Figure 7a, TBA, EtOH, PBQ, and L-histidine were added as the quencher agents of $\cdot OH$, $SO_4^{-}\cdot$ along with $\cdot OH$, $O_2^{-}\cdot$, and $^1O_2$, respectively [59,60]. The addition of 0.12 M TBA or 0.06 mM PBQ reduced the RhB removal efficiency slightly from 100% to 97.1% and 96.1%, respectively. It can be surmised that the hydroxyl radicals ($\cdot OH$) are not the main reactive radicals, and the superoxide radical does not work well. In comparison, the decomposition efficiency of RhB decreased from 100% to 71.4% within 30min when 0.12 M EtOH was added (n_{EtOH}:n_{PMS} = 2000:1). By combining the fact that TBA did not quench the reaction significantly, it can be deduced that it was $SO_4^{-}\cdot$ rather than $\cdot OH$ contributing to the degradation. Specifically, the addition of 0.06 mM L- histidine exhibited an impressive competitive inhibition effect, which made the RhB degrade only 14.1% within 30 min, suggesting that $^1O_2$ could also be a key intermediate together with $SO_4^{-}\cdot$. According to the above analysis, the $SO_4^{-}\cdot$ radical and the singlet oxygen had a great effect on the system.

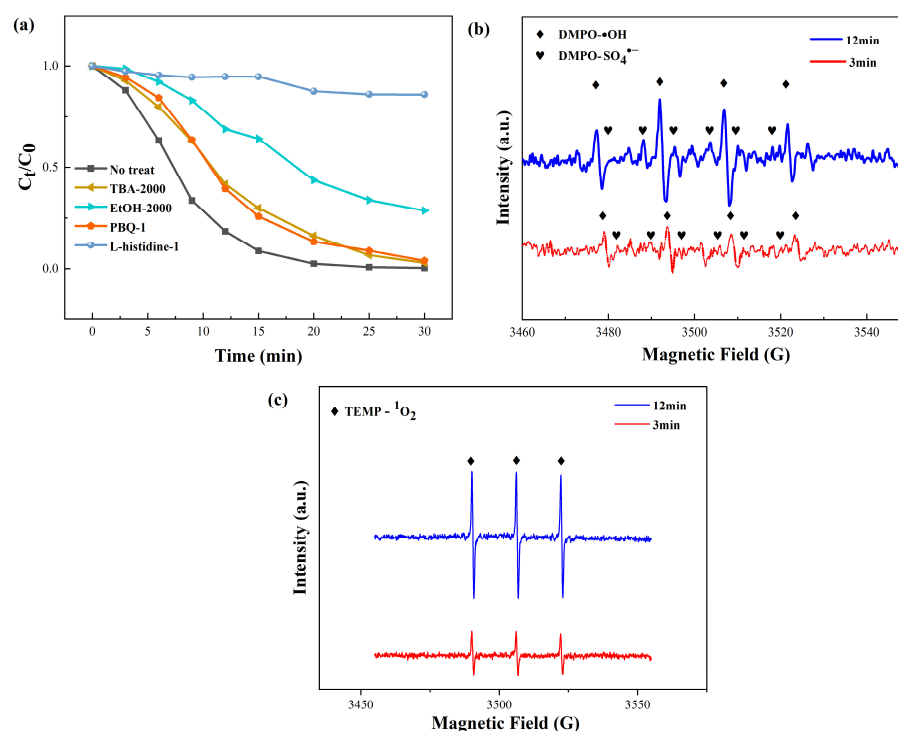**Figure 7.** (**a**) Quenching tests in the $SrCo_{0.5}Mn_{0.5}O_3$–PMS system. (**b**) EPR spectra of DMPO-radical adducts and (**c**) singlet oxygen in the $SrCo_{0.5}Mn_{0.5}O_3$–PMS reaction systems.

To further verify the results of the quenching effect, the EPR analysis was tested with the DMPO as a spin-trap agent for the generated $SO_4^{-}\cdot$ radical and the $\cdot OH$ radical, and TEMP for $^1O_2$, respectively [61,62]. As shown in the Figure 7b, the characteristic peaks of the DMPO-$\cdot OH$ adducts (hyperfine splitting constants $\alpha_H = \alpha_N = 14.8$ G) and DMPO-$SO_4^{-}\cdot$ ($\alpha_H = 0.78$ G, $\alpha_H = 1.48$ G, $\alpha_H = 9.6$ G and $\alpha_N = 13.2$ G) in 3 and 12 min were observed in the EPR spectrums, the upward trend in the catalytic process confirmed the sustained generation of active radicals. Meanwhile, the intensity of the DMOH-$\cdot OH$ adduct had a significant enhancement, and the DMOH-$SO_4^{-}\cdot$ had only weak growth, indicating that it was continuously consumed, which caused the slightly left shift with the time [36]. Additionally, as shown in Figure 7c, three-line peaks were detected in the EPR spectrums

with the relative intensities of 1:1:1, which matched well with the signals of the TEMP-$^1O_2$ adduct.

3.6. Catalytic Mechanism in the SrCo$_{0.5}$Mn$_{0.5}$O$_3$–PMS System

To better investigate the reusability of the catalyst, the XPS spectra of the SrCo$_{0.5}$Mn$_{0.5}$O$_3$ were analyzed before and after the four-cycles activity test. Characteristic peaks of cobalt, manganese, oxygen, and strontium were obtained from the wide XPS spectra (Figure 8a), in which a minor N 1*s* signal could be observed in the used catalyst, which could have originated from the decomposition of RhB. The deconvolution results of fresh and used SrCo$_{0.5}$Mn$_{0.5}$O$_3$ perovskites were all displayed in Tables S2 and S3. From the high-resolution XPS spectrum of Co 2p (Figure 8b), the two main peaks at 780.10 eV and 795.3 eV represent Co 2$p_{3/2}$ and Co 2$p_{1/2}$, respectively, with three shake-up satellites of Co ions at around 789.97 eV and 804.29 eV. The Co 2$p_{1/2}$ peaks at 780.10 eV and 795.10 eV were recognized as Co^{3+}, with the energy splitting about 15 eV. After the catalytic cycles, the relative intensity of Co^{2+}/Co^{3+} dropped from 81.01% to 73.73%, which demonstrates that Co^{2+} played a positive role. The Mn 2p peak had significantly split spin-orbit components at the binding energy of 642.00 eV and 653.2 eV. Through the deconvoluted Mn 2p spectra (Figure 8c), two oxidation states at 642.00 eV (Mn^{3+}) and 644.00 eV (Mn^{4+}) accounted for 68.26% and 31.74% and then changed to 71.91% and 28.09% after the reaction. The increase in the ratio of Mn^{4+}/Mn^{3+} and Co^{3+}/Co^{2+} indicated that the redox of the two B-site metals was included in the PMS system.
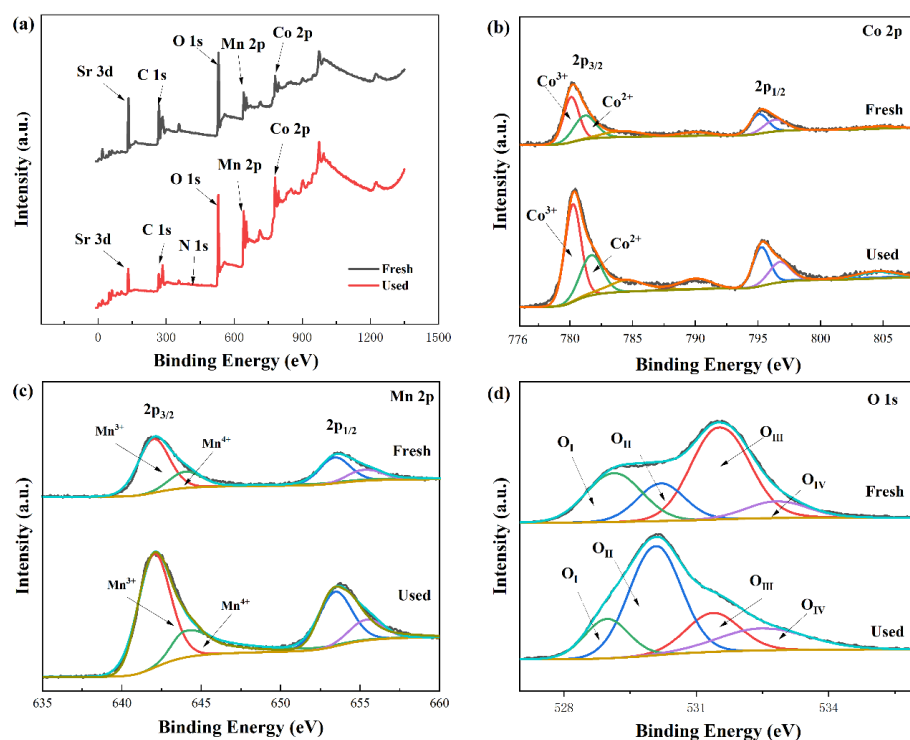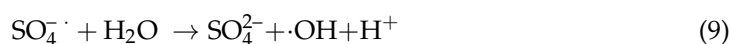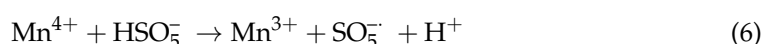

Figure 8. (**a**) survey XPS spectra of fresh and used SrCo$_{0.5}$Mn$_{0.5}$O$_3$ perovskite. (**b–d**) XPS spectra of Co 2p, Mn 2p O 1s of fresh and used SrCo$_{0.5}$Mn$_{0.5}$O$_3$ perovskites.

The high-resolution XPS spectra of O 1 s on SrCo$_{0.5}$Mn$_{0.5}$O$_3$ before and after the reaction were displayed in Figure 8d, in which four oxygen species were found after deconvoluting. Four individual peaks at 529.13 eV, 530.20 eV, 531.50 eV, and 532.8 eV could be regarded as lattice oxygen (O^{2-}, O$_I$), oxygen defects (O$_2^{2-}$/O$^-$, O$_{II}$), surface absorbed oxygen species (O$_{III}$) and adsorbed molecular H$_2$O(O$_{IV}$). The deconvolution results showed that the ratio of O$_{latt}$ had a slight drop of 9.72% and the oxygen species has a sharp decline of 31.09%, suggesting they played an important role in the PMS activation process. Surface-

absorbed oxygen species can improve reactive activity by accelerating the electron transport between PMS and activates through the formation of hydrogen bonds [63]. Meanwhile, the absorbed molecular H_2O increased by 8.72% more than the initial catalyst, which could be owing to the adsorption of organic intermediates in the process.
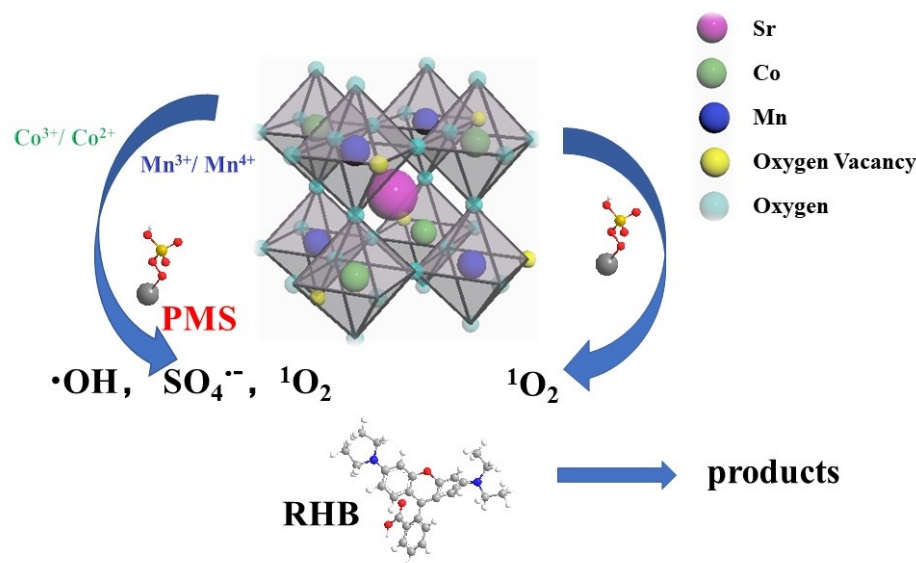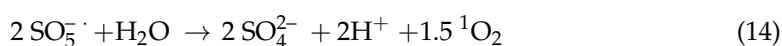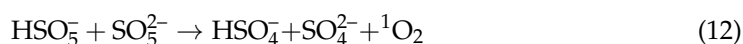
From the discussion above, the two PMS activation mechanisms (radical-based and nonradical processes) on the $SrCo_{0.5}Mn_{0.5}O_3$ perovskite could be proposed as follows (Equations (3)–(15)). In the beginning, the $SO_4^{-\cdot}$ radical was generated through the activation of PMS on activating sites (Co^{2+} and Mn^{3+}) by Equations (3) and (4). The recycling of the redox pair of Co^{3+}/Co^{2+} (1.8 V) could proceed as Equation (5) since it had higher standard redox potentials than that of $SO_5^{-\cdot}/HSO_5^{-}$. Then, the Co^{3+} was reduced to Co^{2+} by the electrons from lattice oxygen. It needs to be noticed that $E^0_{Mn^{4+}/Mn^{3+}}$ (0.15 V) was smaller than HSO_5^{-} ($E^0_{HSO_5^{-\cdot}/SO_5^{-}}$ = 1.1 V), which shows the reduction was thermodynamically favorable (Equation (6)), and $\cdot OH$ also exists through Equations (7)–(9), depending on the actual pH. Meanwhile, the standard redox potential of $E^0_{Mn^{4+}/Mn^{3+}}$(0.15 V) was lower, with a difference of 1.66V than $E^0_{Co^{3+}/Co^{2+}}$ [64]. Therefore, electronic transfer tended to move from Mn^{3+} to Co^{3+} as Equation (10) shows, according to the thermodynamic favorable principles. It was validated by the relatively slight change in Mn valuation and sharp increase of Co^{3+} from the XPS spectra. In addition, the Mn^{4+} was reduced by the neighboring O_L^{2-} as Equation (11) shows [28], which can explain the increase of O_L^{-} and Mn^{3+}. Then, the generated Mn^{3+} could participate in the redox process. Overall, the bimetallic synergistic effects may be seen as the crucial factor to activate PMS since the dopant of Mn cycling of Co-Mn was proven to be more efficient than the $SrCoO_3$ and $SrMnO_3$ perovskites.

$$Co^{2+} + HSO_5^{-} \rightarrow Co^{3+} + SO_4^{-\cdot} + OH^{-}, \tag{3}$$

$$Mn^{3+} + HSO_5^{-} \rightarrow Mn^{4+} + SO_4^{-\cdot} + OH^{-} \tag{4}$$

$$Co^{3+} + HSO_5^{-} \rightarrow Co^{2+} + SO_5^{-\cdot} + H^{+} \tag{5}$$

$$Mn^{4+} + HSO_5^{-} \rightarrow Mn^{3+} + SO_5^{-\cdot} + H^{+} \tag{6}$$

$$Co^{2+}/Mn^{3+} + HSO_5^{-} \rightarrow Co^{3+}/Mn^{4+} \cdot OH + SO_4^{2-} \tag{7}$$

$$SO_4^{-\cdot} + OH^{-} \rightarrow SO_4^{2-} + \cdot OH \tag{8}$$

$$SO_4^{-\cdot} + H_2O \rightarrow SO_4^{2-} + \cdot OH + H^{+} \tag{9}$$

$$Co^{3+} + Mn^{3+} \rightarrow Co^{2+} + Mn^{4+} \quad \Delta E = 1.66\ V \tag{10}$$

$$Mn^{4+} + O_L^{2-} \rightarrow Mn^{3+} + O_L^{-} \tag{11}$$
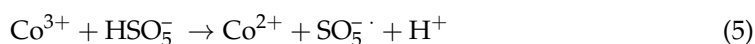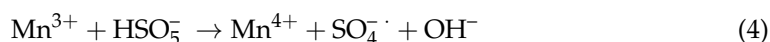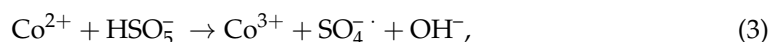
As a high electrophilic reactive oxygen species, singlet oxygen is gradually getting much more attention in recent research [65–67]. In general, singlet oxygen can derive from the decomposition of PMS in suitable pH (near pK_a) [68] as Equation (12) shows. In this work, $^1O_2$ could be generated through metal-based activators [69,70]. The oxygen vacancies could be converted into active oxygen(O^{*}) and further changed into $^1O_2$ (Equation (13)) with PMS. Meanwhile, the generated $SO_5^{-\cdot}$ in the solution could react with H_2O to obtain $^1O_2$ (Equation (14)) also [71]. The $SO_4^{-\cdot}$, $\cdot OH$, and $^1O_2$ radical generated in the $SrCo_{0.5}Mn_{0.5}O_3$–PMS system acted together for RhB degradation. On the whole, the Mn species in the $SrCo_{0.5}Mn_{0.5}O_3$ perovskite not only formed more oxygen vacan-

cies but also participated in PMS activation as activate sites. The possible mechanism in $SrCo_{0.5}Mn_{0.5}O_3$–PMS for removing RhB is depicted in Scheme 1.

$$HSO_5^- + SO_5^{2-} \rightarrow HSO_4^- + SO_4^{2-} + {}^1O_2 \tag{12}$$

$$HSO_5^- + O^* \rightarrow HSO_4^- + {}^1O_2 \tag{13}$$

$$2\,SO_5^{-\cdot} + H_2O \rightarrow 2\,SO_4^{2-} + 2H^+ + 1.5\,{}^1O_2 \tag{14}$$

$${}^1O_2 + SO_4^{-\cdot} + \cdot OH + RhB \rightarrow intermediates \rightarrow CO_2 + H_2O + SO_4^{2-} \tag{15}$$

Scheme 1. A possible mechanism for activation of PMS by $SrCo_{0.5}Mn_{0.5}O_3$.

4. Conclusions

In this work, different $SrCo_xMn_{1-x}O_3$ perovskites were synthesized to catalytically promote the degradation of organic contaminants by SR-AOPs. By adding the Mn element to a similar molar ratio of Co, $SrCo_{0.5}Mn_{0.5}O_3$ still maintained the perovskite structure but has a comparatively higher specific surface area than $SrCoO_3$, and it had more oxygen vacancy than other perovskites. Meanwhile, the $SrCo_{0.5}Mn_{0.5}O_3$ perovskite also showed the highest performance for PMS activation compared to any other catalysts, and the promotion originated from the doping of Mn instead of the appearance of the $SrMnO_3$ phase since the latter performed poorly in PMS activation. Moreover, the stability and reusability were found to perform well and $SrCo_{0.5}Mn_{0.5}O_3$ still had a high activity for RhB removal after four cycles. The B sites composed of Co mixed with Mn were recognized to have a great effect on generating active radicals, which may be explained by two aspects: the generation of singlet oxygen by more oxygen vacancies and the redox cycling between Co and Mn. In the $SrCo_{0.5}Mn_{0.5}O_3$–PMS system, $SO_4^{-\cdot}$, $\cdot OH$, and ${}^1O_2$ were generated and worked together for the degradation of RhB. Our study prepared a high-performance catalyst for AOPs, which had a promising prospect for complex water treatment.

Supplementary Materials: The following supporting information can be downloaded at: https://www.mdpi.com/article/10.3390/pr11041279/s1. Table S1: Lattice parameters of $SrCoO_3$ and $SrCo_{0.5}Mn_{0.5}O_3$ samples. Table S2: the proportion of Co and Mn in fresh and used $SrCo_{0.5}Mn_{0.5}O_3$ perovskite from XPS spectura. Table S3: the proportion of O species in fresh and used $SrCo_{0.5}Mn_{0.5}O_3$ perovskite from XPS spectura. Figure S1: XRD patterens of $SrCo_xMn_{1-x}O_3$ perovskites. Figure S2: Nitrogen adsorption-desorption isotherms of perovskite catalysts with different Mn substituted amounts. Figure S3: EDS mapping spectura of $SrCo_{0.5}Mn_{0.5}O_3$ samples. Figure S4: FT-IR of $SrCo_xMn_{1-x}O_3$ perovskites. Figure S5: Degradation efficience of RhB in the presence of $SrCoO_3$ and PMS alone. Reaction conditions: PMS:0.06 mM, $SrCoO_3$:0.03 g L^{-1}, T = 298 k, pH = 7. Figure S6: pH_{pzc} of $SrCo_{0.5}Mn_{0.5}O_3$ perovskite. Figure S7: UV-VIS spectura of RHB in different time [72–74].

Author Contributions: Conceptualization, P.S., S.H., B.Z. and X.L.; Formal analysis, X.Y., C.Y., S.H., K.L., X.L., K.C., T.L. and J.J.; Investigation, X.Y., C.Y., X.L. and H.H.; Software, P.S., S.H. and B.Z.; Validation, P.S.; Writing—original draft, P.S., C.Y., S.H. and X.L.; Writing—review & editing, X.Y., B.Z., K.L., Z.Y. (Zhenyu Yang), Z.Y. (Zhiwei Yuan), Q.S. and J.R. All authors have read and agreed to the published version of the manuscript.

Data Availability Statement: The data that support the findings of this study are available from the authors, upon reasonable request.

Conflicts of Interest: The authors declare no conflict of interest.

References

1. Muñoz-García, A.B.; Benesperi, I.; Boschloo, G.; Concepcion, J.J.; Delcamp, J.H.; Gibson, E.A.; Meyer, G.J.; Pavone, M.; Pettersson, H.; Hagfeldt, A.; et al. Dye-sensitized solar cells strike back. *Chem. Soc. Rev.* **2021**, *50*, 12450–12550. [CrossRef]
2. Dutta, S.; Gupta, B.; Srivastava, S.K.; Gupta, A.K. Recent advances on the removal of dyes from wastewater using various adsorbents: A critical review. *Mater. Adv.* **2021**, *2*, 4497–4531. [CrossRef]
3. Ardila-Leal, L.D.; Poutou-Pinales, R.A.; Pedroza-Rodriguez, A.M.; Quevedo-Hidalgo, B.E. A Brief History of Colour, the Environmental Impact of Synthetic Dyes and Removal by Using Laccases. *Molecules* **2021**, *26*, 3813. [CrossRef] [PubMed]
4. Ahmad, A.; Mohd-Setapar, S.H.; Chuong, C.S.; Khatoon, A.; Wani, W.A.; Kumar, R.; Rafatullah, M. Recent advances in new generation dye removal technologies: Novel search for approaches to reprocess wastewater. *RSC Adv.* **2015**, *5*, 30801–30818. [CrossRef]
5. Rafaqat, S.; Ali, N.; Torres, C.; Rittmann, B. Recent progress in treatment of dyes wastewater using microbial-electro-Fenton technology. *RSC Adv.* **2022**, *12*, 17104–17137. [CrossRef] [PubMed]
6. Muraro, P.C.L.; Mortari, S.R.; Vizzotto, B.S.; Chuy, G.; Dos Santos, C.; Brum, L.F.W.; da Silva, W.L. Iron oxide nanocatalyst with titanium and silver nanoparticles: Synthesis, characterization and photocatalytic activity on the degradation of Rhodamine B dye. *Sci. Rep.* **2020**, *10*, 3055. [CrossRef]
7. Huang, D.; Zhang, G.; Yi, J.; Cheng, M.; Lai, C.; Xu, P.; Zhang, C.; Liu, Y.; Zhou, C.; Xue, W.; et al. Progress and challenges of metal-organic frameworks-based materials for SR-AOPs applications in water treatment. *Chemosphere* **2021**, *263*, 127672. [CrossRef]
8. Gallego-Ramírez, C.; Chica, E.; Rubio-Clemente, A. Coupling of Advanced Oxidation Technologies and Biochar for the Removal of Dyes in Water. *Water* **2022**, *14*, 2531. [CrossRef]
9. Liu, L.; Chen, Z.; Zhang, J.; Shan, D.; Wu, Y.; Bai, L.; Wang, B. Treatment of industrial dye wastewater and pharmaceutical residue wastewater by advanced oxidation processes and its combination with nanocatalysts: A review. *J. Water Process Eng.* **2021**, *42*, 102122. [CrossRef]
10. Chen, Q.; Ji, F.; Guo, Q.; Guan, W.; Yan, P.; Pei, L.; Xu, X. Degradation of Phenol by Vis/Co-TiO_2/$KHSO_5$ Hybrid Co/SR–Photoprocess at Neutral pH. *Ind. Eng. Chem. Res.* **2013**, *52*, 12540–12549. [CrossRef]
11. Lian, Q.; Roy, A.; Kizilkaya, O.; Gang, D.D.; Holmes, W.; Zappi, M.E.; Zhang, X.; Yao, H. Uniform Mesoporous Amorphous Cobalt-Inherent Silicon Oxide as a Highly Active Heterogeneous Catalyst in the Activation of Peroxymonosulfate for Rapid Oxidation of 2,4-Dichlorophenol: The Important Role of Inherent Cobalt in the Catalytic Mechanism. *ACS Appl. Mater. Interfaces* **2020**, *12*, 57190–57206. [CrossRef] [PubMed]
12. Barndõk, H.; Hermosilla, D.; Negro, C.; Blanco, Á. Comparison and Predesign Cost Assessment of Different Advanced Oxidation Processes for the Treatment of 1,4-Dioxane-Containing Wastewater from the Chemical Industry. *ACS Sustain. Chem. Eng.* **2018**, *6*, 5888–5894. [CrossRef]

13. Qu, J.; Dai, X.; Hu, H.-Y.; Huang, X.; Chen, Z.; Li, T.; Cao, Y.; Daigger, G.T. Emerging Trends and Prospects for Municipal Wastewater Management in China. *ACS EST Eng.* **2022**, *2*, 323–336. [CrossRef]

14. Oh, W.-D.; Dong, Z.; Lim, T.-T. Generation of sulfate radical through heterogeneous catalysis for organic contaminants removal: Current development, challenges and prospects. *Appl. Catal. B Environ.* **2016**, *194*, 169–201. [CrossRef]

15. Li, Z.; Wang, M.; Jin, C.; Kang, J.; Liu, J.; Yang, H.; Zhang, Y.; Pu, Q.; Zhao, Y.; You, M.; et al. Synthesis of novel Co_3O_4 hierarchical porous nanosheets via corn stem and MOF-Co templates for efficient oxytetracycline degradation by peroxymonosulfate activation. *Chem. Eng. J.* **2020**, *392*, 123789. [CrossRef]

16. Lee, Y.C.; Lo, S.L.; Kuo, J.; Huang, C.P. Promoted degradation of perfluorooctanic acid by persulfate when adding activated carbon. *J. Hazard. Mater.* **2013**, *261*, 463–469. [CrossRef]

17. Antoniou, M.G.; de la Cruz, A.A.; Dionysiou, D.D. Degradation of microcystin-LR using sulfate radicals generated through photolysis, thermolysis and e− transfer mechanisms. *Appl. Catal. B Environ.* **2010**, *96*, 290–298. [CrossRef]

18. Chen, M.; Zhu, L.; Liu, S.; Li, R.; Wang, N.; Tang, H. Efficient degradation of organic pollutants by low-level Co^{2+} catalyzed homogeneous activation of peroxymonosulfate. *J. Hazard. Mater.* **2019**, *371*, 456–462. [CrossRef]

19. So, H.-L.; Lin, K.-Y.; Chu, W.; Gong, H. Degradation of Triclosan by Recyclable $MnFe_2O_4$-Activated PMS: Process Modification for Reduced Toxicity and Enhanced Performance. *Ind. Eng. Chem. Res.* **2020**, *59*, 4257–4264. [CrossRef]

20. Yao, Y.; Yang, Z.; Zhang, D.; Peng, W.; Sun, H.; Wang, S. Magnetic $CoFe_2O_4$–Graphene Hybrids: Facile Synthesis, Characterization, and Catalytic Properties. *Ind. Eng. Chem. Res.* **2012**, *51*, 6044–6051. [CrossRef]

21. Lin, N.; Gong, Y.; Wang, R.; Wang, Y.; Zhang, X. Critical review of perovskite-based materials in advanced oxidation system for wastewater treatment: Design, applications and mechanisms. *J. Hazard. Mater.* **2022**, *424*, 127637. [CrossRef] [PubMed]

22. Ji, R.; Chen, J.; Liu, T.; Zhou, X.; Zhang, Y. Critical review of perovskites-based advanced oxidation processes for wastewater treatment: Operational parameters, reaction mechanisms, and prospects. *Chin. Chem. Lett.* **2022**, *33*, 643–652. [CrossRef]

23. Duan, X.; Su, C.; Miao, J.; Zhong, Y.; Shao, Z.; Wang, S.; Sun, H. Insights into perovskite-catalyzed peroxymonosulfate activation: Maneuverable cobalt sites for promoted evolution of sulfate radicals. *Appl. Catal. B Environ.* **2018**, *220*, 626–634. [CrossRef]

24. Xu, X.; Wang, W.; Zhou, W.; Shao, Z. Recent Advances in Novel Nanostructuring Methods of Perovskite Electrocatalysts for Energy-Related Applications. *Small Methods* **2018**, *2*, 1800071. [CrossRef]

25. Xu, X.; Pan, Y.; Ge, L.; Chen, Y.; Mao, X.; Guan, D.; Li, M.; Zhong, Y.; Hu, Z.; Peterson, V.K.; et al. High-Performance Perovskite Composite Electrocatalysts Enabled by Controllable Interface Engineering. *Small* **2021**, *17*, e2101573. [CrossRef]

26. Hammouda, S.B.; Zhao, F.; Safaei, Z.; Srivastava, V.; Lakshmi Ramasamy, D.; Iftekhar, S.; Kalliola, S.; Sillanpää, M. Degradation and mineralization of phenol in aqueous medium by heterogeneous monopersulfate activation on nanostructured cobalt based-perovskite catalysts $ACoO_3$ (A = La, Ba, Sr and Ce): Characterization, kinetics and mechanism study. *Appl. Catal. B Environ.* **2017**, *215*, 60–73. [CrossRef]

27. Pang, X.; Guo, Y.; Zhang, Y.; Xu, B.; Qi, F. $LaCoO_3$ perovskite oxide activation of peroxymonosulfate for aqueous 2-phenyl-5-sulfobenzimidazole degradation: Effect of synthetic method and the reaction mechanism. *Chem. Eng. J.* **2016**, *304*, 897–907. [CrossRef]

28. Luo, X.; Bai, L.; Xing, J.; Zhu, X.; Xu, D.; Xie, B.; Gan, Z.; Li, G.; Liang, H. Ordered Mesoporous Cobalt Containing Perovskite as a High-Performance Heterogeneous Catalyst in Activation of Peroxymonosulfate. *ACS Appl. Mater. Interfaces* **2019**, *11*, 35720–35728. [CrossRef]

29. Jing, J.; Pervez, M.N.; Sun, P.; Cao, C.; Li, B.; Naddeo, V.; Jin, W.; Zhao, Y. Highly efficient removal of bisphenol A by a novel Co-doped $LaFeO_3$ perovskite/PMS system in salinity water. *Sci. Total Environ.* **2021**, *801*, 149490. [CrossRef]

30. Koo, P.-L.; Jaafar, N.F.; Yap, P.-S.; Oh, W.-D. A review on the application of perovskite as peroxymonosulfate activator for organic pollutants removal. *J. Environ. Chem. Eng.* **2022**, *10*, 107093. [CrossRef]

31. Najjar, H.; Batis, H. Development of Mn-based perovskite materials: Chemical structure and applications. *Catal. Rev.* **2016**, *58*, 371–438. [CrossRef]

32. Wang, T.; Qian, X.; Yue, D.; Yan, X.; Yamashita, H.; Zhao, Y. $CaMnO_3$ perovskite nanocrystals for efficient peroxydisulfate activation. *Chem. Eng. J.* **2020**, *398*, 125638. [CrossRef]

33. Lu, S.; Wang, G.; Chen, S.; Yu, H.; Ye, F.; Quan, X. Heterogeneous activation of peroxymonosulfate by $LaCo_{1-x}Cu_xO_3$ perovskites for degradation of organic pollutants. *J. Hazard. Mater.* **2018**, *353*, 401–409. [CrossRef] [PubMed]

34. Pan, Y.; Xu, X.; Zhong, Y.; Ge, L.; Chen, Y.; Veder, J.M.; Guan, D.; O'Hayre, R.; Li, M.; Wang, G.; et al. Direct evidence of boosted oxygen evolution over perovskite by enhanced lattice oxygen participation. *Nat. Commun.* **2020**, *11*, 2002. [CrossRef] [PubMed]

35. Jeerh, G.; Zou, P.; Zhang, M.; Tao, S. Perovskite oxide $LaCr_{0.25}Fe_{0.25}Co_{0.5}O_{3-\delta}$ as an efficient non-noble cathode for direct ammonia fuel cells. *Appl. Catal. B: Environ.* **2022**, *319*, 121919. [CrossRef]

36. Wang, G.; Cheng, C.; Zhu, J.; Wang, L.; Gao, S.; Xia, X. Enhanced degradation of atrazine by nanoscale $LaFe_{1-x}CuxO_3$-delta perovskite activated peroxymonosulfate: Performance and mechanism. *Sci. Total Environ.* **2019**, *673*, 565–575. [CrossRef] [PubMed]

37. Yang, L.; Jiao, Y.; Xu, X.; Pan, Y.; Su, C.; Duan, X.; Sun, H.; Liu, S.; Wang, S.; Shao, Z. Superstructures with Atomic-Level Arranged Perovskite and Oxide Layers for Advanced Oxidation with an Enhanced Non-Free Radical Pathway. *ACS Sustain. Chem. Eng.* **2022**, *10*, 1899–1909. [CrossRef]

38. He, L.; Zhang, Y. Singlet oxygen produced $SrCoO_{2.5}$ in environmental protection: Extraordinary electronic properties and promoted catalytic performance. *J. Sol-Gel Sci. Technol.* **2021**, *99*, 391–401. [CrossRef]

39. Zhang, H.; Zhang, R.; Wu, Z.; Yang, F.; Luo, M.; Yao, G.; Ao, Z.; Lai, B. Cobalt-doped boosted the peroxymonosulfate activation performance of LaFeO3 perovskite for atrazine degradation. *Chem. Eng. J.* **2023**, *452*, 139427. [CrossRef]

40. Chen, H.; Lim, C.; Zhou, M.; He, Z.; Sun, X.; Li, X.; Ye, Y.; Tan, T.; Zhang, H.; Yang, C.; et al. Activating Lattice Oxygen in Perovskite Oxide by B-Site Cation Doping for Modulated Stability and Activity at Elevated Temperatures. *Adv. Sci.* **2021**, *8*, e2102713. [CrossRef]

41. Khazaei, M.; Malekzadeh, A.; Amini, F.; Mortazavi, Y.; Khodadadi, A. Effect of citric acid concentration as emulsifier on perovskite phase formation of nano-sized $SrMnO_3$ and $SrCoO_3$ samples. *Cryst. Res. Technol.* **2010**, *45*, 1064–1068. [CrossRef]

42. Giroir-Fendler, A.; Alves-Fortunato, M.; Richard, M.; Wang, C.; Díaz, J.A.; Gil, S.; Zhang, C.; Can, F.; Bion, N.; Guo, Y. Synthesis of oxide supported $LaMnO_3$ perovskites to enhance yields in toluene combustion. *Appl. Catal. B Environ.* **2016**, *180*, 29–37. [CrossRef]

43. Zhao, L.; Han, T.; Wang, H.; Zhang, L.; Liu, Y. Ni-Co alloy catalyst from $LaNi_{1-x}Co_xO_3$ perovskite supported on zirconia for steam reforming of ethanol. *Appl. Catal. B: Environ.* **2016**, *187*, 19–29. [CrossRef]

44. Mao, W.; Fan, Y.; Hu, X. Degradation of tetrabromobisphenol A through peroxymonaosulfate oxidation activated by $La_{0.5}Sr_{0.5}Co_xMn_{1-x}O_3$-delta perovskite. *Environ. Sci. Pollut. Res. Int.* **2021**, *28*, 65814–65821. [CrossRef]

45. Yang, L.; Hu, R.; Li, H.; Jia, Y.; Zhou, Q.; Wang, H. The effect of interaction between La_2AlCoO_6 and $CuCl_2$ on ethane oxychlorination. *J. Ind. Eng. Chem.* **2017**, *56*, 120–128. [CrossRef]

46. Roozbahani, H.; Maghsoodi, S.; Raei, B.; Kootenaei, A.S.; Azizi, Z. Effects of catalyst preparation methods on the performance of La_2MMnO_6 (M=Co, Ni) double perovskites in catalytic combustion of propane. *Korean J. Chem. Eng.* **2022**, *39*, 586–595. [CrossRef]

47. Li, R.; Zhang, L.; Zhu, S.; Fu, S.; Dong, X.; Ida, S.; Zhang, L.; Guo, L. Layered δ-MnO2 as an active catalyst for toluene catalytic combustion. *Appl. Catal. A Gen.* **2020**, *602*, 117715. [CrossRef]

48. Chen, X.; Zhou, J.; Yang, H.; Wang, H.; Li, H.; Wu, S.; Yang, W. PMS activation by magnetic cobalt-N-doped carbon composite for ultra-efficient degradation of refractory organic pollutant: Mechanisms and identification of intermediates. *Chemosphere* **2022**, *287*, 132074. [CrossRef]

49. Miao, J.; Li, J.; Dai, J.; Guan, D.; Zhou, C.; Zhou, W.; Duan, X.; Wang, S.; Shao, Z. Postsynthesis Oxygen Nonstoichiometric Regulation: A New Strategy for Performance Enhancement of Perovskites in Advanced Oxidation. *Ind. Eng. Chem. Res.* **2019**, *59*, 99–109. [CrossRef]

50. Zhang, W.; Su, Y.; Zhang, X.; Yang, Y.; Guo, X. Facile synthesis of porous $NiCo_2O_4$ nanoflakes as magnetic recoverable catalysts towards the efficient degradation of RhB. *RSC Adv.* **2016**, *6*, 64626–64633. [CrossRef]

51. Yu, H.; Ding, D.; Zhao, S.; Faheem, M.; Mao, W.; Yang, L.; Chen, L.; Cai, T. Co/N co-doped porous carbon as a catalyst for the degradation of RhB by efficient activation of peroxymonosulfate. *Environ. Sci. Pollut. Res.* **2022**, *30*, 10969–10981. [CrossRef] [PubMed]

52. Xu, Z.; Wu, Y.; Ji, Q.; Li, T.; Xu, C.; Qi, C.; He, H.; Yang, S.; Li, S.; Yan, S.; et al. Understanding spatial effects of tetrahedral and octahedral cobalt cations on peroxymonosulfate activation for efficient pollution degradation. *Appl. Catal. B Environ.* **2021**, *291*, 120072. [CrossRef]

53. Tan, J.; Xu, C.; Zhang, X. MOFs-derived defect carbon encapsulated magnetic metallic Co nanoparticles capable of efficiently activating PMS to rapidly degrade dyes. *Sep. Purif. Technol.* **2022**, *289*, 120812. [CrossRef]

54. Wang, L.; Di, J.; Nie, J.; Ma, G. Multicomponent Doped Sugar-Coated Nanofibers for Peroxymonosulfate Activation. *ACS Appl. Nano Mater.* **2019**, *2*, 6998–7007. [CrossRef]

55. Liu, Y.; Tian, X.; Xiong, W.; Nie, G.; Xiao, L. Prussian blue analogs derived nanostructured Mn/Fe bimetallic carbon materials for organic pollutants degradation via peroxymonosulfate activation. *Colloids Surf. A Physicochem. Eng. Asp.* **2023**, *657*, 130592. [CrossRef]

56. Fan, J.; Zhao, Z.; Ding, Z.; Liu, J. Synthesis of different crystallographic FeOOH catalysts for peroxymonosulfate activation towards organic matter degradation. *RSC Adv.* **2018**, *8*, 7269–7279. [CrossRef]

57. Yang, Z.; Duan, X.; Wang, J.; Li, Y.; Fan, X.; Zhang, F.; Zhang, G.; Peng, W. Facile Synthesis of High-Performance Nitrogen-Doped Hierarchically Porous Carbon for Catalytic Oxidation. *ACS Sustain. Chem. Eng.* **2020**, *8*, 4236–4243. [CrossRef]

58. Zhang, H.; Zhou, C.; Zeng, H.; Shi, Z.; Wu, H.; Deng, L. Novel sulfur vacancies featured MIL-88A(Fe)@CuS rods activated peroxymonosulfate for coumarin degradation: Different reactive oxygen species generation routes under acidic and alkaline pH. *Process Saf. Environ. Prot.* **2022**, *166*, 11–22. [CrossRef]

59. Liang, P.; Zhang, C.; Duan, X.; Sun, H.; Liu, S.; Tade, M.O.; Wang, S. N-Doped Graphene from Metal–Organic Frameworks for Catalytic Oxidation of p-Hydroxylbenzoic Acid: N-Functionality and Mechanism. *ACS Sustain. Chem. Eng.* **2017**, *5*, 2693–2701. [CrossRef]

60. Zhu, M.; Miao, J.; Duan, X.; Guan, D.; Zhong, Y.; Wang, S.; Zhou, W.; Shao, Z. Postsynthesis Growth of CoOOH Nanostructure on $SrCo_{0.6}Ti_{0.4}O_{3-δ}$ Perovskite Surface for Enhanced Degradation of Aqueous Organic Contaminants. *ACS Sustain. Chem. Eng.* **2018**, *6*, 15737–15748. [CrossRef]

61. Wang, L.; Fu, Y.; Li, Q.; Wang, Z. EPR Evidence for Mechanistic Diversity of Cu(II)/Peroxygen Oxidation Systems by Tracing the Origin of DMPO Spin Adducts. *Environ. Sci. Technol.* **2022**, *56*, 8796–8806. [CrossRef] [PubMed]

62. Huang, B.C.; Huang, G.X.; Jiang, J.; Liu, W.J.; Yu, H.Q. Carbon-Based Catalyst Synthesized and Immobilized under Calcium Salt Assistance To Boost Singlet Oxygen Evolution for Pollutant Degradation. *ACS Appl. Mater. Interfaces* **2019**, *11*, 43180–43187. [CrossRef] [PubMed]

63. Yu, D.; He, J.; Xie, T.; Yang, J.; Wang, J.; Xie, J.; Shi, H.; Gao, Z.; Xiang, B.; Dionysiou, D.D. Boosting catalytic activity of $SrCoO_{2.52}$ perovskite by Mn atom implantation for advanced peroxymonosulfate activation. *J. Hazard. Mater.* **2023**, *442*, 130085. [CrossRef]

64. Xu, Y.; Hu, E.; Xu, D.; Guo, Q. Activation of peroxymonosulfate by bimetallic CoMn oxides loaded on coal fly ash-derived SBA-15 for efficient degradation of Rhodamine B. *Sep. Purif. Technol.* **2021**, *274*, 119081. [CrossRef]

65. Zhu, M.; Miao, J.; Guan, D.; Zhong, Y.; Ran, R.; Wang, S.; Zhou, W.; Shao, Z. Efficient Wastewater Remediation Enabled by Self-Assembled Perovskite Oxide Heterostructures with Multiple Reaction Pathways. *ACS Sustain. Chem. Eng.* **2020**, *8*, 6033–6042. [CrossRef]

66. Li, X.; Wang, L.; Guo, Y.; Song, W.; Li, Y.; Yan, L. Goethite-MoS_2 hybrid with dual active sites boosted peroxymonosulfate activation for removal of tetracycline: The vital roles of hydroxyl radicals and singlet oxygen. *Chem. Eng. J.* **2022**, *450*, 138104. [CrossRef]

67. Shao, S.; Li, X.; Gong, Z.; Fan, B.; Hu, J.; Peng, J.; Lu, K.; Gao, S. A new insight into the mechanism in Fe_3O_4@CuO/PMS system with low oxidant dosage. *Chem. Eng. J.* **2022**, *438*, 135474. [CrossRef]

68. Zhou, Y.; Jiang, J.; Gao, Y.; Ma, J.; Pang, S.Y.; Li, J.; Lu, X.T.; Yuan, L.P. Activation of Peroxymonosulfate by Benzoquinone: A Novel Nonradical Oxidation Process. *Environ. Sci. Technol.* **2015**, *49*, 12941–12950. [CrossRef]

69. Zhu, S.; Li, X.; Kang, J.; Duan, X.; Wang, S. Persulfate Activation on Crystallographic Manganese Oxides: Mechanism of Singlet Oxygen Evolution for Nonradical Selective Degradation of Aqueous Contaminants. *Environ. Sci. Technol.* **2019**, *53*, 307–315. [CrossRef]

70. Bu, Y.; Li, H.; Yu, W.; Pan, Y.; Li, L.; Wang, Y.; Pu, L.; Ding, J.; Gao, G.; Pan, B. Peroxydisulfate Activation and Singlet Oxygen Generation by Oxygen Vacancy for Degradation of Contaminants. *Environ. Sci. Technol.* **2021**, *55*, 2110–2120. [CrossRef]

71. Yang, S.; Zhang, S.; Li, X.; Du, Y.; Xing, Y.; Xu, Q.; Wang, Z.; Li, L.; Zhu, X. One-step pyrolysis for the preparation of sulfur-doped biochar loaded with iron nanoparticles as an effective peroxymonosulfate activator for RhB degradation. *New J. Chem.* **2022**, *46*, 5678–5689. [CrossRef]

72. Zhao, P.; Fang, F.; Feng, N.; Chen, C.; Liu, G.; Chen, L.; Zhu, Z.; Meng, J.; Wan, H.; Guan, G. Self-templating construction of mesopores on three dimensionally ordered macroporous $La_{0.5}Sr_{0.5}MnO_3$ perovskite with enhanced performance for soot combustion. *Catal. Sci. Technol.* **2019**, *9*, 1835–1846. [CrossRef]

73. Zhao, S.; Wang, L.; Wang, Y.; Li, X. Hierarchically porous $LaFeO_3$ perovskite prepared from the pomelo peel bio-template for catalytic oxidation of NO. *J. Phys. Chem. Solids* **2018**, *116*, 43–49. [CrossRef]

74. Demirel, S.; Oz, E.; Altin, S.; Bayri, A.; Baglayan, O.; Altin, E.; Avci, S. Structural, magnetic, electrical and electrochemical properties of $SrCoO_{2.5}$, $Sr_9Co_2Mn_5O_{21}$ and $SrMnO_3$ compounds. *Ceram. Int.* **2017**, *43*, 14818–14826. [CrossRef]